JACS
JOURNAL OF THE AMERICAN CHEMICAL SOCIETY

Article

pubs.acs.org/JACS

Side-Chain Conducting and Phase-Separated Polymeric Binders for High-Performance Silicon Anodes in Lithium-Ion Batteries

Sang-Jae Park,[†,⊥] Hui Zhao,[†,⊥] Guo Ai,[†,§] Cheng Wang,[‡] Xiangyun Song,[†] Neslihan Yuca,[∥] Vincent S. Battaglia,[†] Wanli Yang,[‡] and Gao Liu*[,†]

[†]Environmental Energy Technologies Division and [‡]Advanced Light Source, Lawrence Berkeley National Laboratory, Berkeley, California 94720, United States

[§]Science and Technology on Reliability Physics and Application of Electronic Component Laboratory, Guangzhou 510610, Guangdong, P.R. China

[∥]Istanbul Technical University, Energy Institute, Istanbul 34469, Turkey

Supporting Information

ABSTRACT: Here we describe a class of electric-conducting polymers that conduct electrons via the side chain $\pi-\pi$ stacking. These polymers can be designed and synthesized with different chemical moieties to perform different functions, extremely suitable as a conductive polymer binder for lithium battery electrodes. A class of methacrylate polymers based on a polycyclic aromatic hydrocarbon side moiety, pyrene, was synthesized and applied as an electrode binder to fabricate a silicon (Si) electrode. The electron mobilities for PPy and PPyE are characterized as 1.9×10^{-4} and 8.5×10^{-4} $cm^2\ V^{-1}\ s^{-1}$, respectively. These electric conductive polymeric binders can maintain the electrode mechanical integrity and Si interface stability over a thousand cycles of charge and discharge. The as-assembled batteries exhibit a high capacity and excellent rate performance due to the self-assembled solid-state nanostructures of the conductive polymer binders. These pyrene-based methacrylate binders also enhance the stability of the solid electrolyte interphase (SEI) of a Si electrode over long-term cycling. The physical properties of this polymer are further tailored by incorporating ethylene oxide moieties at the side chains to enhance the adhesion and adjust swelling to improve the stability of the high loading Si electrode.

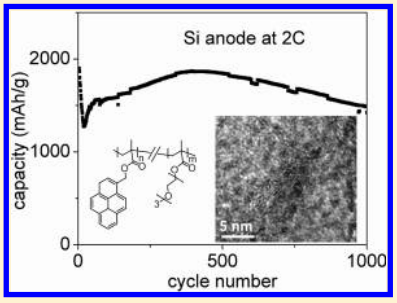

INTRODUCTION

Lithium-ion batteries are changing the pattern of energy consumption in our daily life by enabling long-driving-range electric vehicles and the storage of renewable energy in our utility grids.[1−3] Much research haas focused on the development of high-capacity active materials and components to enhance the energy density and performance of the next generation of lithium-ion batteries.[4−8] Of those, silicon (Si) is theoretically expected to have 10 times higher capacity (ca. 4200 mAh/g) than that of the current graphite anode (ca. 370 mAh/g).[9,10] However, the practical applications of silicon for the anode electrode have been hindered due to severe volume change during repetitive lithiation and delithiation cycles that results in the loss of the electrical contacts and the fast capacity fading.[11,12] Another leading factor of Si electrode degradation is the continuous side reactions of electrolyte on the Si surface due to the volume change of the Si particle.[13,14] Meanwhile, a challenge for the practical application of electrodes that consist of silicon materials is how to increase the mass loading and area-specific capacity to increase the entire cell's practical energy density.[15−17] Electrodes with high mass loading of Si tend to cycle very poorly, due to shrinkage of electrode porosity during lithiation of Si particles. The large expansion and contraction of the Si particles lead to electrode disintegration during cycling.[18,19] Though silicon nanoparticles and polymeric binders based on the polysaccharides (like CMC) have been used to alleviate the stress during cell cycling,[20−23] their performance has not met the critical requirements for practical application (e.g., long cycle life, high mass loading, high Coulombic efficiency, and so on). Recent work has demonstrated that the polymeric binders with high electronic conductivity and mechanical binding force can be used for silicon anodes to achieve high-capacity and long-term cycles without adding conductive carbon.[24,25] That work indicates that development of conductive polymeric binders could be critical for the practical application of silicon anodes. The conventional conductive polymers consist of highly conjugated, rigid backbones based on sp^2 carbon to produce conjugated structure. The conjugated structures in the conductive polymer are critical for long-range mobility of polarons. The synthesis of the polymer backbone conjugated conductive polymers usually proceeds through complex coupling reactions that require the noble metal catalysts and stringent reaction conditions, making future structure modification very complex and costly. Herein we describe the development of a versatile synthetic process for the next generation of pyrene-based polymeric binders with high solubility and very flexible backbone structures along the

Received: October 31, 2014
Published: February 3, 2015

DOI: 10.1021/ja511181p
J. Am. Chem. Soc. 2015, 137, 2565−2571

chains. The reaction proceeds through the free-radical polymerization of the methacrylate backbone. The polymerization process does not require the transition metal catalyst and has relaxed requirements to the experimental condition. The electric conductive moiety is at the branch/side chain structure of the polymer. The polymer structure can be easily modified to incorporate certain functional groups into the side structures, in order to tailor the polymer adhesion and swelling properties.

RESULTS AND DISCUSSION

Side-Chain Conducting Polymeric Binders. Polycyclic aromatic hydrocarbons, including anthracene and pyrene, are organic semiconductors and have been used in optoelectronic devices due to their high electrical conductivity and fluorescent properties.[26,27] When the pyrene molecules are connected to flexible backbones along the chain, they are close in position to be easily self-assembled into ordered structures, to further enhance the electrical conductivity by the $\pi-\pi$ stacking force of the aromatic moieties.[28−30] The flexible backbone structures facilitate strong interaction between the pyrene units and the silicon nanoparticles. In addition, the side chain structure of pyrene and flexible backbone increase the processability (such as solubility) and lower the solution viscosity. Pyrene-based polymers were synthesized via free-radical polymerization (Figure 1a). The radical-based polymerization is a versatile process compared with that of conventional sp^2 carbon coupling reaction using noble metal catalysts. The functional groups, such as carboxylic acid, hydroxyl, and amino groups can be easily incorporated into the polymer structures without compromising the polymerization reaction process. Because different active materials have different physical and chemical properties (especially on the surface), the easy tailoring of the polymer properties by the incorporation of specific functional groups extends the versatility of these polymers over the various electrode materials and applications. A pyrene-based homopolymer poly(1-pyrenemethyl methacrylate) (PPy) was synthesized and investigated. The PPy has the pyrene groups for electric conducting only. A copolymer, poly(1-pyrenemethyl methacrylate-*co*-triethylene oxide methyl ether methacrylate) (PPyE), with ethylene oxide functional groups was also synthesized, and it contains an electric-conducting pyrene moiety and triethylene oxide units for better adhesion and for improving swelling.[31,32] First, the monomer, 1-pyrenemethyl methacrylate, was synthesized by the reaction of 1-pyrenemethanol and methacryloyl chloride. For the PPy homopolymer, the monomers were initiated with 2,2′-azobis (2-methylpropionitrile) (AIBN) to proceed via free-radical polymerization. For the PPyE copolymer, 1-pyrenemethyl methacrylate was mixed with triethylene oxide methyl ether methacrylate (E moiety) and initiated by AIBN for copolymer synthesis.

Phase-Separated Polymer Morphologies. The as-synthesized polymers are self-assembled into the ordered structures by $\pi-\pi$ interaction of pyrene units on the chain. Transmission electron microscopy (TEM) was used to study the self-assembled structures. Figure 1b and c shows the ordered nanostructures for both PPy and PPyE. PPy self-assembled into a long-range order structure, whereas PPyE assembled into ordered and amorphous domains intertwined together. Since the homopolymer of poly(triethylene oxide methyl ether methacrylate) (E) is an amorphous structure at room temperature, the amorphous domains of PPyE are from the aggregation of triethylene oxide, and the ordered domains

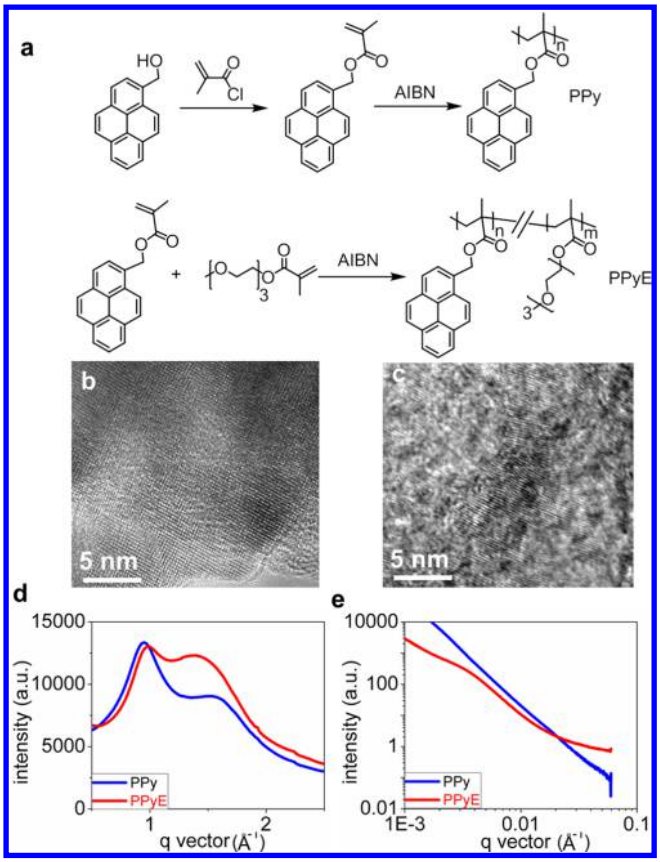

Figure 1. (a) Generic synthesis of poly(1-pyrenemethyl methacrylate) (PPy, top) and poly(1-pyrenemethyl methacrylate-*co*-triethylene oxide methyl ether methacrylate) (PPyE, bottom). (b) High-resolution TEM (HRTEM) images of PPy polymer. (c) HRTEM of PPyE polymer. (d) Wide angle X-ray scattering (WAXS) of PPy and PPyE polymers. (e) Resonant soft X-ray scattering (RsoXS) spectra of PPy and PPyE polymers.

are from pyrene aggregates. However, the distance of the lattice fringes is higher in PPyE polymer than that of the PPy homopolymer, due to the increased disorder produced by the introduction of triethylene oxide moieties. Wide-angle X-ray scattering (WAXS) results show the ordered phase characteristic of the pyrene in both PPy and PPyE. Diffraction peaks are located at ∼0.95 and ∼0.98 $Å^{-1}$, respectively. This corresponding lattice spacing of ∼0.6 nm agrees with the electron microscopy result. The broadening of the diffraction peak for the PPyE sample indicates that the crystal grain size is smaller when copolymerized with E moieties (Figure 1d). Resonant soft X-ray scattering (RSoXS) was used to study the nanophase separation in the PPy and PPyE samples. RSoXS uses soft X-ray energies near the carbon k-edge, where it has enhanced chemical contrast for the polymer/polymer system.[33,34] The longer wavelength allows it to probe a large range, from a few micrometers to a few nanometers. A broad scattering peak oberserved at ∼0.003 $Å^{-1}$ indicates that there is a correlation length between domains on the order of 200 nm. There is no such feature in the neat PPy sample (Figure 1e). It is very intriguing that the pyrene and E moieties form the domain structure in the PPyE polymer, although PPyE is a random copolymer. This correlation is most likely between the ordered region and the amorphous region of PPyE. The intermixing of conductive pyrene between the ordered region and the amorphous region of the PPyE ensures the existence of

DOI: 10.1021/ja511181p
J. Am. Chem. Soc. 2015, 137, 2565−2571

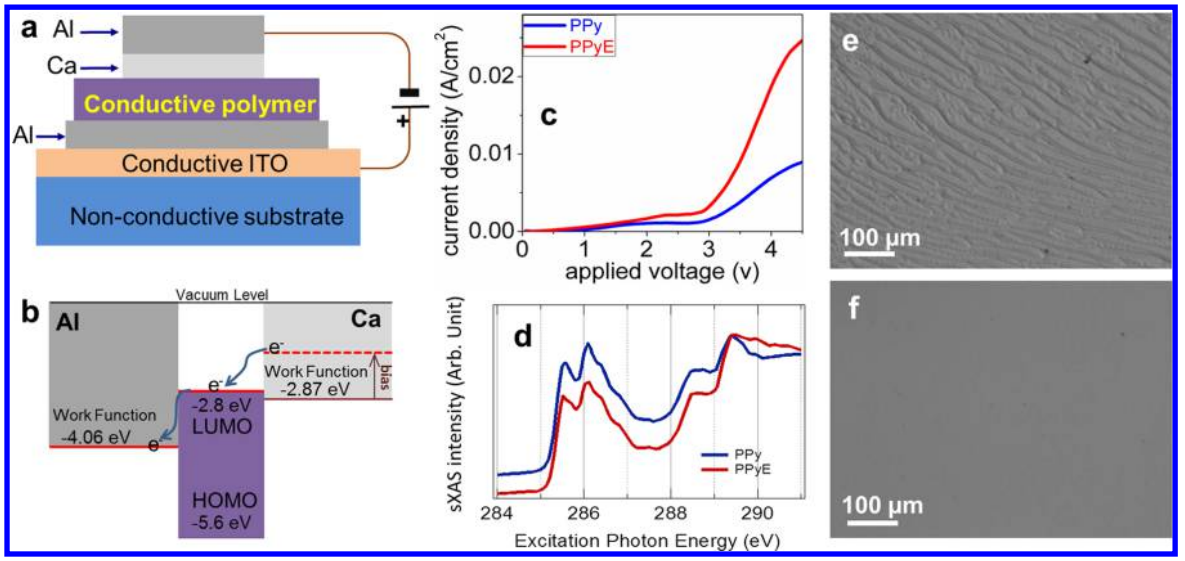

Figure 2. Improvement of the electron mobility in PPyE. (a) Schematic cross section of the electron mobility testing device with ITO/Al/conductive binder/Ca/Al. (b) Corresponding energy diagram; values of energy levels are adapted from ref 35. (c) $J-V$ characteristics of PPy and PPyE at room temperature. (d) Carbon k-edge sXAS of PPy and PPyE shows that the LUMO energy is intact in PPyE, although nonconductive ethylene oxide groups are introduced. (e, f) Optical images of PPy and PPyE films, respectively, deposited on silicon wafers.

continuing and uncompromised conductive path for electrons. The existence of the amorphous PPyE domains with an elastic component E improves adhesion with the Si particle surface and electrolyte uptake, and hence the Li-ion transport.[31,35,36] Therefore, the nanoscale phase separation maintains electric conduction and enhances ionic conductivities and adhesion of the PPyE binder to improve the electrode performance based on this binder.

Improved Electron Mobility of the Conductive Polymer. The phase-separated morphology shown in TEM facilitates electron mobility and electronic conductivity. Steady-state space-charge-limited-current (SCLC) method is used to measure the electron mobility. It is based on a current density (J) to applied voltage (V) characteristics in the dark condition. The $J-V$ characteristics of the device depend on the device characteristics and preparation techniques such as material, device configuration, electrode work function, applied electrical field, and so forth. When the device conditions are fixed or known, the $J-V$ characteristics can be used to calculate electron mobility and conductivity of the conductive polymer. The $J-V$ characteristics of PPy and PPyE are measured with the device depicted in Figure 2a. The energy diagram of our measurements is plotted in Figure 2b, with the values of energy levels from ref 35. Because the work function of Ca is close to the LUMO state of the conductive polymers, electrons will flow from the Ca to the Al electrodes through the conductive polymer even with a small bias voltage. The $J-V$ curves (Figure 2c) thus represent the mobility of the electrons flowing through our conductive polymers.

At low voltage, the $J-V$ curves are linear, showing a typical ohmic behavior, which corresponds to the thermally generated free carriers through the device. The number of injected charge carriers is negligible compared to the thermal carrier. The current density can be described by Ohm's law:

$$J = \frac{q\mu_n n_0 V}{d}$$

where q is the charge of the electron, μ_n is the electron mobility, n_0 the number of the charge carriers, V is the applied voltage, and d is the sample thickness. When the applied voltages further increases beyond the potential barrier, the current prefers injection limited model instead of transport-limited model, and the $J-V$ characteristics are dominated by space-charge limited current, given by the Mott–Gurney law:

$$J = \frac{9}{8}\varepsilon_0\varepsilon_r\mu_n\frac{(V - V_{bi})^3}{L^3}$$

where ε_0 and ε_r indicate the absolute permittivity and relative permittivity of polymer, μ_n is the mobility, V is the applied voltage, V_{bi} is the built-in potential, and L is for the film thickness.

Figure 2c shows that, overall, both PPyE and PPy have high electron mobility.[37] The values of electron mobility of PPy and PPyE obtained by fitting the experimental data are 1.9×10^{-4} and 8.5×10^{-4} $cm^2\ V^{-1}\ s^{-1}$, respectively. The copolymer of PPyE displays much higher electron mobility than that of PPy, which could be seen directly in Figure 2c. This improvement on electron mobility is intriguing because the ethylene oxide group in PPyE are nonconducting and one would expect a worse electron mobility in PPyE compared with PPy.

In order to understand the improved electron mobility in PPyE, we studied the electronic structure of both the PPy and PPyE polymers with synchrotron-based X-ray absorption spectroscopy (sXAS). sXAS is a direct probe of the excitations of core level electrons to the unoccupied states. Previously, we have demonstrated that sXAS could be employed to study the electric properties of polymer materials efficiently.[24,32] The methodology is based on the fact that the lowest-energy sXAS feature directly corresponds to the state of lowest unoccupied molecular orbital (LUMO), which is very sensitive to the electric property of the polymers.[38] Figure 2d shows the sXAS of PPy and PPyE. The splitting peaks around 285–286 eV correspond to the $\pi^*_{C=C}$ bonds with conjugation, and the features around 288 eV are from $\pi^*_{C=O}$.[38] Detailed analysis of the sXAS features is not a topic of this work. Here we focus on the low-energy sXAS features corresponding to the LUMO states. It is obvious that incorporating the ethylene oxide group in PPyE does not change the lowest-energy features in sXAS,

DOI: 10.1021/ja511181p
J. Am. Chem. Soc. 2015, 137, 2565–2571

indicating the LUMO of the PPy polymer is intact in PPyE. The consistency of the overall line shape also implies that the electron states close to the Fermi level is dominated by the pyrene-based PPy states. This comparison is thus reliable without core-hole potential concerns.[24]

Therefore, the improvement of electron mobility in PPyE stems from the morphology optimization through the E groups, instead of a fundamental electronic structure change. Incorporating the E moiety improves the uniformity of the PPyE film. As shown by the optical images of the polymer films deposited on silicon wafers (Figure 2e and f), the PPyE indeed forms a very uniform film, while grain boundaries of the separated domains could be easily seen for the PPy film. We argue that the electron mobility is hindered by the grain boundaries in PPy. The E moiety, although nonconductive, optimizes the overall morphology of PPyE by forming uniform film without large grain boundary, leading to higher electron mobility.

Electrochemical Performance. The electrodes (Si/PPy and Si/PPyE) were prepared by using Si nanoparticles and the PPy or PPyE polymers without any conductive additives (Si to polymer weight ratio = 2:1). The scanning electron microscopy (SEM) image of the as-prepared Si/PPy electrode before cycling (Figure 3b) shows the uniform laminate structure and

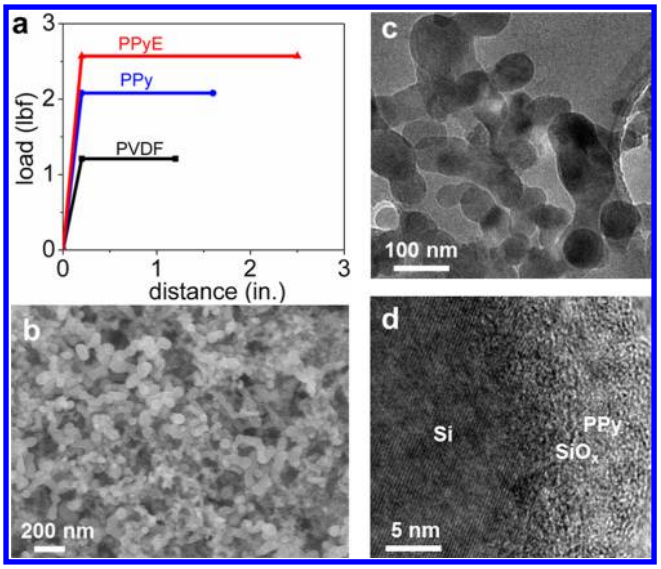

Figure 3. (a) Peel test results of the PPy-, PPyE-, and PVDF-based Si electrodes. (b) SEM image of the pristine PPy/Si electrode. (c and d) TEM images of the pristine PPy/Si electrode.

surface porosities that facilitate the easy access of lithium ions and electrolyte during cell cycling.[39] The TEM morphology in Figure 3c indicates the uniform and thin layer of polymer binder coated on the surface of Si nanoparticles. This architecture facilitates both electron transport and lithium ion conductivity after swelled by the electrolytes.

The assembled coin cells (mass loading = 0.15−0.3 mg/cm^2 silicon nanoparticles) were cycled at a C/10 rate (C/n rate corresponds to the charge and discharge of a cell in n hours) (Figure 4a). The Si/PPy and Si/PPyE cells show the stable cycle performance and high capacity (2100 mAh/g for PPy and 2300 mAh/g for PPyE after 180 cycles). The first-cycle voltage curves are shown in Figure 4b, the Coulombic efficiencies for both polymers are similar, 67.82% for PPy and 70.70% for PPyE. The average Coulombic efficiency for long-term cycling

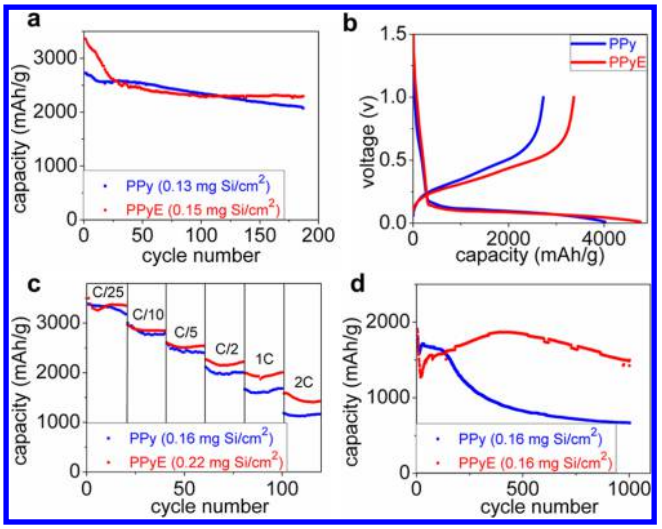

Figure 4. (a) Charge (delithiation) capacities of PPy- and PPyE-based Si electrodes at $C/10$. (b) First-cycle voltage curves. (c) Rate performance. (d) Charge (delithiation) capacities of PPy- and PPyE-based Si electrodes at $2C$ rate. Mass loadings of Si for each cell are labeled in the plot.

is higher in the Si/PPyE electrode (99.5%) than in the Si/PPy electrode (98.3%) (Supporting Information Figure S3). This is due to increased adhesion of the PPyE binder to the Si because of the E moiety in the PPyE. The coverage of PPyE on Si is more effective during volume change of the Si nanoparticle, which could be indicated from the optical image of the polymer films in Figure 2d and e. The high Coulombic efficiencies of Si/PPy and Si/PPyE demonstrate that the SEI layers are stable, and the electrolyte decomposition on the Si surface is slowed during cycles. The thin SEI layer also contributes to the significantly improved charge and discharge rate (high current density) performance. The coin cells exhibit good rate capability at a high current density (Figure 4c). Even at a $2C$ cycling rate, they retain high capacity; the capacity based on PPyE retains ∼1500 mAh/g after 1000 cycles $2C$ rate (Figure 4d). The good performance at the fast charging and discharging rate indicates that the pyrene-based polymers have enough high electric conductivity to eliminate the conductive carbon and to increase the overall energy density. The PPy solid-state ordered packing plays a critical role to facilitate the charge transport in the conductive polymer binders.

Although the above electrochemical performance is based on an electrode with 33% binder, higher loading of Si active materials is preferred toward a high-energy cell design. As shown in Figure S5, the Si content could be as high as 95% in the electrode laminate, the cycling performance still maintains stability, which further shows the advantageous of PPy-based binder. Because of the huge volume expansion, the electrodes with high mass loading and a thick layer would not endure the stress and retain the electrical contact during cell cycling. To investigate the effect of higher mass loading, the thicker Si/PPy electrode (mass loading = 1.0 mg/cm^2) was prepared and the porosity of the electrode was optimized. The electrochemical performance of this high-loading electrode is shown in Figure S7; the high areal capacity at ∼2.5 mAh/cm^2 indicates that the pyrene-based conductive polymers could attain a high-energy electrode for practical anode applications.

The SEM images of the Si electrodes after long-term cycling are shown in Figure 5c and d. Compared to the conventional Si

DOI: 10.1021/ja511181p
J. Am. Chem. Soc. 2015, 137, 2565−2571

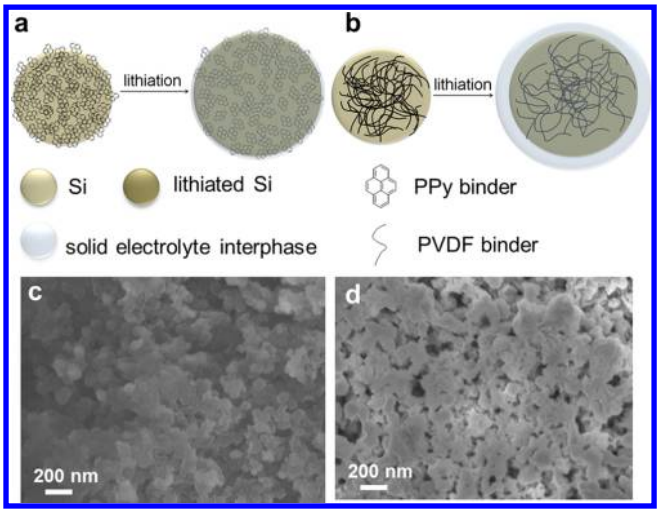

Figure 5. Schematics showing volume change of silicon nanoparticle covered by (a) PPy and (b) conventional polymeric binders, and the SEI layer during cycling. SEM images of the (c) PPy and (d) PVDF electrodes after 500 cycles at 1*C*.

nanoparticle electrode with a nonconductive binder (PVDF), the decomposition layer on the PPy/Si electrode was much thinner. The Si nanoparticles were still individually visible after 500 cycles of deep charge and discharge. In a conventional Si electrode with PVDF binder, the continuous volume change of Si particles makes the stable SEI formation impossible. The volume expansion of Si during lithiation exposes new Si surfaces, leading to additional SEI formation and more side reaction products. However, during delithiation, the Si particles shrink, and the SEI crumbles from the Si surface.[40,41] These processes cause the formation of a thick layer of organic species due to the continuous decomposition of the electrolyte (Figure 5d).[42] In contrast, the Si nanoparticle and PPy conductive binder based electrode has a much thinner SEI layer after repeated cycles, and SEI growth is very minimal. The spherical shapes of Si particles are clearly visible with very minimum size changes after 500 cycles (Figure 5c). The Si/PPy electrode has 33% PPy binder to entirely cover the Si particle surfaces. Due to the electric conductivity of the pyrene, the SEI is formed on the surface of the PPy binder instead of on the Si surface directly. Since the polymer tends to have higher free volume, the PPy binder provides volume stability during Si volume expansion and contraction. PPy polymers completely cover the surface of the silicon nanoparticles during the volume change (Figure 5a), which reduces the contact between the silicon nanoparticles and the electrolyte, and the continuous consumption of the electrolyte is hindered. Therefore, the SEI on the Si/PPy electrode is much more stable compared to the SEI on the conventional composite. This is also confirmed by the high Coulombic efficiency of 99.5% during long-term cycling.

■ CONCLUSION

In summary, a new type of side-chain electron-conducting polymer binder was developed. These polymers can be synthesized via a versatile free-radical polymerization process, allowing easy incorporation of functional groups to fine-tune the binder's properties. When pyrenes are used as conducting side chains, the pyrene moieties are self-assembled into structures with long-range ordering, enhancing the electron conduction in the electrode. The pyrene-based conductive polymer binder helps to form a stable SEI layer for the Si electrode. When the cells consisting of silicon nanoparticles and polymers have been cycled, they show the stable and high capacities even at a fast cycle rate, such as 2*C*. The functional groups such as E can be easily incorporated as a part of the polymer structure. The electrodes consisting of the pyrene and E enable higher mass loading of Si with stable cycling performance.

Recent development of high-capacity anodes for lithium-ion battery indicates that, instead of using pure silicon as anode materials, the use of silicon-containing materials, such as SiOx,[43] Si/C,[44] and Si alloy,[45] shows better promise toward a practical application in LIBs. The polymer structure and approach developed here can be used to tailor the physical and chemical properties of polymers in the advanced electrode design for different high-energy materials with different surface morphology and chemistry, while not sacrificing electronic conductivity.

■ METHODS

Synthesis. *1-Pyrenemethyl Methacrylate.* 1-Pyrenemethanol (30 g) was dissolved in freshly distilled tetrahydrofuran (THF, 280 mL). Triethylamine (28 mL) and pyridine (18 mL) were added to the solution, and the mixture was cooled to 0 °C. Then methacryloyl chloride (19 mL) was added dropwise. After the addition, the ice–water bath was removed and the mixture was stirred for 1 h. After water (75 mL) was added to the reaction flask, the solution was transferred into a separatory funnel and extracted with diethyl ether (500 mL). The extract was washed with aqueous HCl (1 M, 150 mL), aqueous $NaHCO_3$ (5%, 150 mL), and brine (150 mL). The solvent was evaporated in a vacuum and recrystallized with methanol. (Product: 27 g.) ^{1}H NMR (500 MHz, $CDCl_3$): δ 8.35 (d, J = 9.2 Hz, 1H), 8.25 (t, J = 6.6 Hz, 2H), 8.21 (d, J = 9.8 Hz, 2H), 8.12 (t, J = 4.6 Hz, 3H), 8.06 (m, 1H), 6.18 (s, 1H), 5.95 (s, 2H), 5.59 (s, 1H), 2.00 (s, 3H) ppm.

Poly(1-pyrenemethyl methacrylate) (PPy). 1-Pyrenemethyl methacrylate (1.2 g) was dissolved in freshly distilled THF (4 mL). To the solution, 2,2′-azobis(2-methylpropionitrile) (AIBN, 8 mg) was added. The mixture was degassed by three freeze–evacuate–thaw cycles and heated to 60 °C for 24 h. The product was purified by precipitation with diethyl ether. (Product: 1.1 g.) ^{1}H NMR (500 MHz, $CDCl_3$): δ 7.48 (br), 5.09 (br), 1.80 (br), 0.71 (br) ppm. GPC ($CHCl_3$, polystyrene standards, M_n = 21 000, PDI = 2.5)

Poly(1-pyrenemethyl methacrylate-co-triethylene oxide methyl ether methacrylate) (PPyE). 1-Pyrenemethyl methacrylate (5.0 g) and triethylene oxide methyl ether methacrylate (1.7 g) were dissolved in freshly distilled THF (15 mL). To the solution, AIBN (20 mg) was added. The mixture was degassed by three freeze–evacuate–thaw cycles and heated to 60 °C for 24 h. The product was purified by precipitation with diethyl ether. (Product: 4.0 g.) ^{1}H NMR (500 MHz, $CDCl_3$): δ 7.71 (br), 5.37 (br), 3.96 (br), 3.26 (br), 1.83 (br), 0.79 (br) ppm. GPC ($CHCl_3$, polystyrene standards, M_n = 34 000, PDI = 2.9)

Electron Microscopy Measurements. SEM images of the composite electrode surface were collected with a JEOL JSM-7500F field emission scanning electron microscope with an accelerating voltage of 15 kV using the high vacuum mode at room temperature. The electrode surface chemistry was analyzed with EDXA from Thermo Scientific Analysis. High-resolution TEM images were obtained on a Philips CM200 field emission microscope operated at 200 kV at the National Center for Electron Microscopy (NCEM) at Lawrence Berkeley National Laboratory (LBNL).

X-ray Scattering Measurements.[46] A WAXS experiment was performed at the ALS Beamline 7.3.3. Hard X-rays of 10 keV were used. Samples were pressed into a 1 mm pellet. Two-dimensional WAXS data were collected using a Platus 1 M detector. A resonant soft

DOI: 10.1021/ja511181p
J. Am. Chem. Soc. 2015, 137, 2565–2571

X-ray scattering (RSoXS) experiment was carried out at the ALS Beamline 11.0.1.2. Samples were drop-cast on silicon nitride (Si_3N_4) membranes (Norcada) with a 5 mm × 5 mm frame and a 1 mm × 1 mm window size and dried in a vacuum oven at 90 °C for 12 h. The X-ray transmits through a 100 nm membrane thickness. The sample thickness was about 1 μm. RSoXS data were collected at photon energies close to the carbon k-edge (~280 eV) to achieve good contrast between polymers.

Soft X-ray Absorption Spectroscopy. sXAS was performed at Beamline 9.0.1 of the Advanced Light Source (ALS) at Lawrence Berkeley National Laboratory (LBNL). The undulator and spherical grating monochromators supply a linearly polarized photon beam with resolving power up to 6000.[47] The experimental energy resolution is 0.1 eV without considering core-hole broadening. Data were collected in both total electron yield (TEY) and total fluorescence yield (TFY) modes simultaneously, corresponding to a probe depth of about 10 nm (for TEY) and 100 nm (for TFY). Only TEY data are shown here, and TFY data show the same results. All the spectra have been normalized to the beam flux measured by the upstream gold mesh. In order to avoid radiation damage of the samples, the sXAS experiments are performed with liquid N_2 cooling at 80 K. The soft X-ray beam is defocused through a specific bendable X-ray mirror to reduce the brightness, until the spectra are confirmed to be free of radiation damage features after multiple scans.

Preparation of Electrodes and Assembly of Coin Cells. All the electrodes and coin cells were prepared and assembled in the Ar-filled glovebox. The polymers were dissolved in NMP, and then silicon nanoparticles were added (weight ratio of Si nanoparticle/polymer = 2:1). The mixture was mixed by using a homogenizer for 1 h, and the slurry was coated on the copper foil by using a doctor blade. The coated electrode was placed in the glovebox overnight and further dried in the vacuum oven at 90 °C for 12 h to completely remove the NMP solvents. The electrodes were used to assemble the coin cells. Polypropylene separators (Celgard 2400) and the electrolyte (BASF) consisting of 1.2 M lithium hexafluorophosphate ($LiPF_6$) in ethylene carbonate (EC), diethyl carbonate (DEC) (EC/DEC = 3:7 by weight), and 30% by weight of fluoroethylene carbonate (FEC) were added. As a counter electrode, the Li metal was used. The assembled cells were placed on the channels (Maccor Inc.) at 30 °C for lithiation−delithiation cycles. Cyclic voltammetry (CV) was executed by using a Biologic Instrument.

■ ASSOCIATED CONTENT

Ⓢ Supporting Information

Experimental details, Figures S1−S10. This material is available free of charge via the Internet at http://pubs.acs.org

■ AUTHOR INFORMATION

Corresponding Author

*gliu@lbl.gov

Author Contributions

⊥S.-J.P. and H.Z. contributed equally to this work.

Notes

The authors declare no competing financial interest.

■ ACKNOWLEDGMENTS

This work was supported by the Assistant Secretary for Energy Efficiency and Renewal Energy under the Advanced Battery Materials Research (BMR) program and by University of California, Office of the President through the University of California Discovery Grant program. Transmission electron microscopy was performed at the National Center for Electron Microscopy (NCEM), soft X-ray scattering and analysis at the Advanced Light Source (ALS), and nuclear magnetic resonance spectroscopy (NMR) analyses at the Molecular Foundry—all located at Lawrence Berkeley National Laboratory and supported by the Director, Office of Science, Office of Basic Energy Sciences, of the U.S. Department of Energy under Contract No. DE-AC02-05CH11231. G.A. is supported by the China Scholarship Council Fellowship.

■ REFERENCES

(1) Tarascon, J. M.; Armand, M. *Nature* **2001**, *414*, 359.
(2) Thackeray, M. M.; Wolverton, C.; Isaacs, E. D. *Energy Environ. Sci.* **2012**, *5*, 7854.
(3) Goodenough, J. B.; Park, K. S. *J. Am. Chem. Soc.* **2013**, *135*, 1167.
(4) Whittingham, M. S. *Chem. Rev.* **2004**, *104*, 4271.
(5) Xu, K. *Chem. Rev.* **2004**, *104*, 4303.
(6) Bruce, P. G.; Scrosati, B.; Tarascon, J. M. *Angew. Chem., Int. Ed.* **2008**, *47*, 2930.
(7) Goodenough, J. B.; Kim, Y. *Chem. Mater.* **2010**, *22*, 587.
(8) Choi, N. S.; Chen, Z. H.; Freunberger, S. A.; Ji, X. L.; Sun, Y. K.; Amine, K.; Yushin, G.; Nazar, L. F.; Cho, J.; Bruce, P. G. *Angew. Chem., Int. Ed.* **2012**, *51*, 9994.
(9) Boukamp, B. A.; Lesh, G. C.; Huggins, R. A. *J. Electrochem. Soc.* **1981**, *128*, 725.
(10) Li, J.; Dahn, J. R. *J. Electrochem. Soc.* **2007**, *154*, A156.
(11) Ryu, J. H.; Kim, J. W.; Sung, Y. E.; Oh, S. M. *Electrochem. Solid-State Lett.* **2004**, *7*, A306.
(12) Christensen, J.; Newman, J. *J. Solid State Electrochem.* **2006**, *10*, 293.
(13) Ryu, Y.-G.; Lee, S.; Mah, S.; Lee, D. J.; Kwon, K.; Hwang, S.; Doo, S. *J. Electrochem. Soc.* **2008**, *155*, A583.
(14) Song, S.-W.; Baek, S.-W. *Electrochem. Solid-State Lett.* **2009**, *12*, A23.
(15) Liu, N.; Lu, Z.; Zhao, J.; McDowell, M. T.; Lee, H.-W.; Zhao, W.; Cui, Y. *Nat. Nanotechnol.* **2014**, *9*, 187.
(16) Song, J.; Zhou, M.; Yi, R.; Xu, T.; Gordin, M. L.; Tang, D.; Yu, Z.; Regula, M.; Wang, D. *Adv. Funct. Mater.* **2014**, *24*, 5904.
(17) Yi, R.; Zai, J.; Dai, F.; Gordin, M. L.; Wang, D. *Nano Energy* **2014**, *6*, 211.
(18) Beattie, S. D.; Larcher, D.; Morcrette, M.; Simon, B.; Tarascon, J.-M. *J. Electrochem. Soc.* **2008**, *155*, A158.
(19) Renganathan, S.; Sikha, G.; Santhanagopalan, S.; White, R. E. *J. Electrochem. Soc.* **2010**, *157*, A155.
(20) Bridel, J. S.; Azais, T.; Morcrette, M.; Tarascon, J. M.; Larcher, D. *Chem. Mater.* **2010**, *22*, 1229.
(21) Kovalenko, I.; Zdyrko, B.; Magasinski, A.; Hertzberg, B.; Milicev, Z.; Burtovyy, R.; Luzinov, I.; Yushin, G. *Science* **2011**, *334*, 75.
(22) Koo, B.; Kim, H.; Cho, Y.; Lee, K. T.; Choi, N. S.; Cho, J. *Angew. Chem., Int. Ed.* **2012**, *51*, 8762.
(23) Ryou, M. H.; Kim, J.; Lee, I.; Kim, S.; Jeong, Y. K.; Hong, S.; Ryu, J. H.; Kim, T. S.; Park, J. K.; Lee, H.; Choi, J. W. *Adv. Mater.* **2013**, *25*, 1571.
(24) Liu, G.; Xun, S. D.; Vukmirovic, N.; Song, X. Y.; Olalde-Velasco, P.; Zheng, H. H.; Battaglia, V. S.; Wang, L. W.; Yang, W. L. *Adv. Mater.* **2011**, *23*, 4679.
(25) Wu, M.; Sabisch, J. E. C.; Song, X.; Minor, A. M.; Battaglia, V. S.; Liu, G. *Nano Lett.* **2013**, *13*, 5397.
(26) Nakada, I.; Ichimiya, A.; Ariga, K. *J. Phys. Soc. Jpn.* **1964**, *19*, 1587.
(27) Martinez-Manez, R.; Sancenon, F. *Chem. Rev.* **2003**, *103*, 4419.
(28) Oh, H.-Y.; Lee, C.; Lee, S. *Org. Electron.* **2009**, *10*, 163.
(29) Liu, F.; Xie, L.-H.; Tang, C.; Liang, J.; Chen, Q.-Q.; Peng, B.; Wei, W.; Cao, Y.; Huang, W. *Org. Lett.* **2009**, *11*, 3850.
(30) Zhang, Q.; Divayana, Y.; Xiao, J.; Wang, Z.; Tiekink, E. R. T.; Doung, H. M.; Zhang, H.; Boey, F.; Sun, X. W.; Wudl, F. *Chem.—Eur. J.* **2010**, *16*, 7422.
(31) Hochgatterer, N. S.; Schweiger, M. R.; Koller, S.; Raimann, P. R.; Wöhrle, T.; Wurm, C.; Winter, M. *Electrochem. Solid-State Lett.* **2008**, *11*, A76.
(32) Wu, M.; Xiao, X.; Vukmirovic, N.; Xun, S.; Das, P. K.; Song, X.; Olalde-Velasco, P.; Wang, D.; Weber, A. Z.; Wang, L.-W.; Battaglia, V. S.; Yang, W.; Liu, G. *J. Am. Chem. Soc.* **2013**, *135*, 12048.

DOI: 10.1021/ja511181p
J. Am. Chem. Soc. 2015, 137, 2565−2571

(33) Chen, W.; Xu, T.; He, F.; Wang, W.; Wang, C.; Strzalka, J.; Liu, Y.; Wen, J.; Miller, D. J.; Chen, J.; Hong, K.; Yu, L.; Darling, S. B. *Nano Lett.* **2011**, *11*, 3707.
(34) Liu, F.; Wang, C.; Baral, J. K.; Zhang, L.; Watkins, J. J.; Briseno, A. L.; Russell, T. P. *J. Am. Chem. Soc.* **2013**, *135*, 19248.
(35) Fongy, C.; Gaillot, A.-C.; Jouanneau, S.; Guyomard, D.; Lestriez, B. *J. Electrochem. Soc.* **2010**, *157*, A885.
(36) Fongy, C.; Jouanneau, S.; Guyomard, D.; Badot, J. C.; Lestriez, B. *J. Electrochem. Soc.* **2010**, *157*, A1347.
(37) Trattnig, R.; Pevzner, L.; Jäger, M.; Schlesinger, R.; Nardi, M. V.; Ligorio, G.; Christodoulou, C.; Koch, N.; Baumgarten, M.; Müllen, K.; List, E. J. W. *Adv. Funct. Mater.* **2013**, *23*, 4897.
(38) Stohr, J. *NEXAFS Spectroscopy*; Springer Science & Business Media: Berlin, Heidelberg, New York, 1992.
(39) Zhao, H.; Zhou, X.; Park, S.-J.; Shi, F.; Fu, Y.; Ling, M.; Yuca, N.; Battaglia, V.; Liu, G. *J. Power Sources* **2014**, *263*, 288.
(40) Liu, Y.; Matsumura, T.; Imanishi, N.; Hirano, A.; Ichikawa, T.; Takeda, Y. *Electrochem. Solid-State Lett.* **2005**, *8*, A599.
(41) Chew, S. Y.; Guo, Z. P.; Wang, J. Z.; Chen, J.; Munroe, P.; Ng, S. H.; Zhao, L.; Liu, H. K. *Electrochem. Commun.* **2007**, *9*, 941.
(42) Shi, F.; Zhao, H.; Liu, G.; Ross, P. N.; Somorjai, G. A.; Komvopoulos, K. *J. Phys. Chem. C* **2014**, *118*, 14732.
(43) Zhang, L.; Deng, J.; Liu, L.; Si, W.; Oswald, S.; Xi, L.; Kundu, M.; Ma, G.; Gemming, T.; Baunack, S.; Ding, F.; Yan, C.; Schmidt, O. G. *Adv. Mater.* **2014**, *26*, 4527.
(44) Du, Z.; Dunlap, R. A.; Obrovac, M. N. *J. Electrochem. Soc.* **2014**, *161*, A1698.
(45) Chevrier, V. L.; Liu, L.; Le, D. B.; Lund, J.; Molla, B.; Reimer, K.; Krause, L. J.; Jensen, L. D.; Figgemeier, E.; Eberman, K. W. *J. Electrochem. Soc.* **2014**, *161*, A783.
(46) Gann, E.; Young, A. T.; Collins, B. A.; Yan, H.; Nasiatka, J.; Padmore, H. A.; Ade, H.; Hexemer, A.; Wang, C. *Rev. Sci. Instrum.* **2012**, *83*, 045110.
(47) Jia, J. J.; Callcott, T. A.; Yurkas, J.; Ellis, A. W.; Himpsel, F. J.; Samant, M. G.; Stöhr, J.; Ederer, D. L.; Carlisle, J. A.; Hudson, E. A.; Terminello, L. J.; Shuh, D. K.; Perera, R. C. C. *Rev. Sci. Instrum.* **1995**, *66*, 1394.

DOI: 10.1021/ja511181p
J. Am. Chem. Soc. 2015, 137, 2565−2571